Energetic Neutral Atom (ENA) emission characteristics at the Moon and Mercury from 3D regolith simulations of solar wind reflection

P.S. Szabo[1], A.R. Poppe[1], A. Mutzke[2], S. Fatemi[3], A. Vorburger[4], P. Wurz[4]

[1]Space Sciences Laboratory, University of California, Berkeley, USA
[2]Max Planck Institute for Plasma Physics (IPP), Greifswald, Germany
[3]Department of Physics, Umeå University, Umeå, Sweden
[4]Physics Institute, University of Bern, Bern, Switzerland

Key Points:

- We model the solar wind proton reflection from lunar regolith grains to study energetic neutral atom (ENA) emission characteristics.
- ENA emission angles are successfully connected to the regolith geometry, while ENA energies are mostly determined by the solar wind energy.
- Expanding the model to Mercury, we predict ENA fluxes that will be observed by BepiColombo.

Corresponding author: Paul S. Szabo, szabo@berkeley.edu

Abstract

The reflection of solar wind protons as energetic neutral atoms (ENAs) from the lunar surface has regularly been used to study the plasma-surface interaction at the Moon. However, there still exists a fundamental lack of knowledge of the scattering process. ENA emission from the surface is expected to similarly occur at Mercury and will be studied by BepiColombo. Understanding this solar wind backscattering will allow studies of both Mercury's plasma environment as well as properties of the hermean surface itself. Here, we expand on previous simulation studies of the solar-wind-regolith interaction with 3D grains in SDTrimSP-3D to compare the predicted scattering energies and angles to ENA measurements from the Moon by the Chandrayaan-1 and IBEX missions. The simulations reproduce a backward emission towards the Sun, which can be connected to the geometry of the regolith grain stacking. In contrast, the ENA energy distribution and its Maxwellian shape is mostly connected to the solar wind velocity. Our simulations also correctly describe a lunar ENA albedo between 10% and 20% and support its decrease with solar wind velocity. We further expand our studies to illustrate how BepiColombo will be able to observe ENAs at Mercury using hybrid simulations of Mercury's magnetosphere as an input for the complex surface precipitation patterns. We demonstrate that the variable ion precipitation will directly influence ENA emission from the surface. The orbits of BepiColombo's MPO and MMO/Mio spacecraft are shown to be suitable to observe ENA emission patterns both on a local and a global scale.

Plain Language Summary

The Sun emits a continuous stream of charged particles, the solar wind. Recently, it was observed that these solar wind particles get reflected from the Moon in a similar way as it is the case for light from the Sun. The reflection is the result of a large number of collisions between the solar wind particles and atoms at the Moon's surface. This is expected to occur similarly at the planet Mercury. To better understand this process, we present a theoretical model of the reflection process. Our simulations take into account all the collisions with atoms, as well as the geometry of the lunar soil as a large number of loosely stacked grains. The model achieves very good agreement with most of the observations from the Moon, showing that sunward scattering and the scattering probability can be explained by the porous regolith. Consequently, we also sketch how particle scattering would occur at Mercury, where the solar wind only reaches the sur-

face at select locations due to the planet's magnetic field. Our results confirm the variability of the scattered particles around Mercury and that the BepiColombo mission is well-suited to observe them for imaging solar wind impacts onto the surface.

1 Introduction

The surfaces of planetary bodies that are not protected by an atmosphere are typically exposed to ion precipitation from different sources. This has especially been of interest to understand how those ion impacts contribute to space weathering and change the observable surface (Pieters & Noble, 2016). Analysis of atoms sputtered from the surface, which can form a tenuous exosphere, can also give remote insights into the surface composition (Wurz et al., 2022). Another key aspect in the ion-surface interaction is the measurement of Energetic Neutral Atoms (ENAs) from neutralized and reflected ions that precipitate the surface. This effect leads to significant fluxes of ENAs emitted from the surface at 100s of eV and was first observed at the Moon about 15 years ago (McComas et al., 2009; Wieser et al., 2009). Total reflection probabilities as well as scattering angles and energies have largely been characterized at the Moon (Schaufelberger et al., 2011; Futaana et al., 2012; Funsten et al., 2013; Vorburger et al., 2013; Lue et al., 2016). However, a fundamental theoretical description of the backscattering process that precisely reproduces all of these characteristics has not yet been established. Such understanding is essential to extrapolate findings from the Moon to other planetary bodies to better understand how they interact with their plasma environments. For the scattering of a precipitating solar wind ion, the whole process will be affected by the impactor as well as the target surface. ENA studies thus provide a promising opportunity to study properties of both precipitation as well as properties of the surface.

It had long been known that the Moon emits sputtered neutral atoms at an energy range of eV to 10s of eV (Wurz et al., 2007). However, measurements by the Earth-orbiting IBEX mission and the Chandrayaan-1 lunar orbiter revealed an additional high-energy hydrogen ENA population (McComas et al., 2009; Wieser et al., 2009). This could be explained by solar wind protons being backscattered and neutralized during the interaction with regolith grains at the surface of the Moon. The main reason for this conclusion were the ENA energies at 100s of eV and the observation that these energies are strongly correlated with the solar wind ion energies (Wieser et al., 2009; Futaana et al., 2012). Measurements of the ENA scattering function have revealed a preferential sunward emission (Schaufelberger et al., 2011; Vorburger et al., 2013), possibly connected to the geometry of the porous regolith. Total solar wind proton backscattering coefficients, i.e., the probability of backscattering, were measured to be between 10 and 20% (Rodriguez M. et al., 2012; Vorburger et al., 2013; Funsten et al., 2013). ENAs have also been shown

to be useful in remotely observing the general characteristics of lunar magnetic anomalies (Wieser et al., 2010; Futaana et al., 2013), with the surface magnetization seemingly being the main driver of local variability in the ENA flux from backscattered protons (Vorburger et al., 2015). Furthermore, ENA emission has been observed from interaction of the Moon with terrestrial plasma populations (Harada et al., 2014; Lue et al., 2017). A small component of precipitating protons was also found to be backscattered as charged particles: Kaguya, Chandrayaan-1 and ARTEMIS have shown that the probability of this process is below 1% (Saito et al., 2008; Lue et al., 2014, 2018). Backscattered protons tend to have larger energies than backscattered neutral atoms, consistent with the view that they mostly undergo fewer interatomic collisions before being fully reflected (Lue et al., 2018).

While so far only extensively observed at the Moon, similar ion backscattering processes can be assumed to occur at other atmosphereless bodies in the solar system. Measurements of backscattered protons from the Martian moon Phobos have been attempted with the Mars Express and MAVEN spacecraft (Futaana et al., 2010, 2021; Deniau et al., 2022), leading to inconclusive results. Low fluxes of reflected charged particles, electromagnetic fields that affect ion paths, and the Martian hydrogen exosphere as a potential additional source of protons complicate the observation. It will likely require orbital measurements from JAXA's Martian Moons eXploraion (MMX) mission to provide definitive insights into the proton backscattering from Phobos (Yokota et al., 2021; Kuramoto et al., 2022).

Such problems are less likely to arise when studying ENAs and this represents an exciting opportunity for Mercury and its upcoming studies by the BepiColombo mission (Benkhoff et al., 2010, 2021). The solar system's smallest and innermost planet has so far remained a relatively unexplored destination. It has only been the target of two missions in NASA's Mariner 10 and MESSENGER spacecraft (Strom, 1979; Solomon et al., 2018). The BepiColombo mission (Benkhoff et al., 2010), launched in 2018 and jointly operated by ESA and JAXA, is currently on its cruise to Mercury and will enter its final orbit in late 2025 to start its full science campaign. First flyby results have been reported (Harada et al., 2022; Orsini et al., 2022; Alberti et al., 2023; Chaufray et al., 2023), but the full capabilities of the spacecraft will only be available after the deployment of its two modules, the Mercury Planetary Orbiter (MPO) and the Mercury Magnetospheric Orbiter (MMO or Mio). Both spacecraft will observe Mercury from polar orbits, which

will allow full coverage to study the planet's interior, its surface and its environment (Benkhoff et al., 2021).

Similar to its predecessors, BepiColombo does not include a lander and our understanding of Mercury is thus further strongly connected to remote analysis methods. As it is done for the Moon (Poppe et al., 2022), one important method for investigating Mercury's surface has been the analysis of the exosphere around the planet (Killen et al., 2007), allowing insights into composition and surface processes. It is populated by release of atoms from the surface and here sputtering by ion impacts represents a key driver for some species (Wurz et al., 2022). In contrast to the Moon, Mercury's internal magnetic field causes a much more complicated interaction of the planet with the solar wind plasma (Slavin et al., 2008) and prevents impacts on large parts of the hermean dayside surface (Kallio & Janhunen, 2003; Sarantos et al., 2007; Winslow et al., 2014). Instead, precipitation is expected to be more localized on polar cusps at high day side latitudes (Raines et al., 2022), polar horns (Glass et al., 2022), or the night side (Benna et al., 2010). Precipitating ion fluxes are typically lower than the solar wind flux (Winslow et al., 2014; Fatemi et al., 2020; Raines et al., 2022; Glass et al., 2022) and ion energies are expected to vary between significantly smaller than the solar wind ion energy up to several keV (Fatemi et al., 2020; Glass et al., 2022). Learning more about the surface of Mercury is thus strongly connected to establishing a full understanding of the plasma-surface interaction to constrain precipitating fluxes of solar wind ions and magnetospheric species. This will also help to inform the extent of space weathering that is to be expected in Mercury's unique environment (Domingue et al., 2014), which affects the state of the planetary surface that we observe today. Here ENA measurements can give direct insights into the location, fluxes, energies and species of ions impacting the surface (Vorburger et al., 2012). Both BepiColombo's MPO and MMO spacecraft are equipped with the necessary scientific instruments to perform energy- and direction-resolved ENA observations (Orsini et al., 2021; Saito et al., 2021). The surface precipitation findings can thus be particularly expected to make ENA measurements an important tool to better describe Mercury's magnetosphere and its interaction with Mercury's surface.

As an opportunity for additional insights, it can be anticipated that several regolith properties influence the ENA emission. Investigating samples with scattered ions at keV energies is a common method for laboratory analysis techniques. For example, Low Energy Ion Scattering (LEIS) spectroscopy can be used to derive surface composition from

scattering energies and angles (Niehus et al., 1993). Recently, Helium Ion Microscopy (HIM) has also emerged as an instrument for high-resolution imaging from scattered ions (Hlawacek et al., 2014). However, conditions for plasma-surface interactions in space are typically far from those in an idealized laboratory setup. To deduce surface properties from ENA measurements, a model will be required that is able to simulate the interaction of precipitating ions with the regolith grains on a planetary surface. Only then will it become feasible to fully relate ENA characteristics to properties of either the precipitating ions or the ion-impact exposed surface.

First theoretical approaches were explored by Hodges (2011) showing that backscattered energies can be explained by multiple interatomic collisions between solar wind protons and regolith grains. However, total reflection coefficients were significantly over-estimated and scattering angles were not discussed. Recently, we have developed a regolith-model for the ion-surface interaction code SDTrimSP-3D to model ENA backscattering coefficients from the Moon in excellent agreement with Chandrayaan-1 measurements (Szabo, Poppe, et al., 2022). Leblanc et al. (2023) also studied lunar ENAs, applying a combination of a Molecular Dynamics (MD) simulation with a Monte Carlo code to model intergranular transport, which led to reasonable agreement with scattering coefficients and energies.

With our model (Szabo, Poppe, et al., 2022), we have previously shown that the total backscattering coefficient depends on regolith porosity, reproducing Chandrayaan-1 data for its angular dependence with fairy-castle like, highly porous regolith. Ultimately, the lunar regolith porosity at the surface could be constrained to $0.85^{+0.15}_{-0.14}$. This agreed with the value from Hapke and Sato (2016), which was derived for the Apollo 16 site to be 0.83 ± 0.03. However, our result is valid on a global scale and did not require analysis of returned samples, demonstrating one example for the capability of surface studies with ENAs.

In this paper, we extend our simulations of the solar wind proton reflection to focus on scattering angles and energies of the emitted ENAs and compare results from our SDTrimSP-3D regolith model to measurements from Chandrayaan-1 and IBEX. Using this approach, scattering angles are found to reproduce the main feature of the measured ENA scattering function, i.e., a preferential sunwards reflection. We confirm that this is due to shadowing effects connected to the regolith geometry. ENA energies also mostly agree well with the Chandrayaan-1 energy spectra, and our simulations confirm that ENA

energies are strongly dependent on the energies of the precipitating solar wind protons. At different solar wind velocities we also find a decrease of the lunar ENA albedo that agrees very well with reports from IBEX data. Finally, we simulate ENA fluxes around Mercury based on inputs from our ion-regolith interaction model and precipitation fluxes from plasma-hybrid models of the hermean magnetosphere. In doing so, we demonstrate how the complex precipitation patterns cause variable ENA emissions and that the orbit of the BepiColombo mission will be well-suited to study both local precipitation patterns as well as ENA emission on a global scale.

2 SDTrimSP-3D for Solar Wind-Regolith Interaction

The impact and subsequent scattering of solar wind protons from planetary regolith is modeled with the SDTrimSP-3D code (Von Toussaint et al., 2017). SDTrimSP-3D represents an expansion of the Binary Collision Approximation (BCA) simulation software SDTrimSP (Mutzke et al., 2019), which has primarily been developed for studying plasma-wall interaction in nuclear fusion research. Recently, this program has also been applied to space weathering studies to simulate solar wind sputtering yields (Schaible et al., 2017; Szabo et al., 2020) or space weathering effects (Christoph et al., 2022). Within the BCA, the ion's path through a solid and all collisions of the projectile as well as any recoil atoms are fully calculated in a sequential manner. This is achieved by modeling the scattering of two atoms using a screened interatomic potential, while the electronic stopping is implemented from tabulated values or empirical models. This approach neglects multi-body collisions and overlapping collision cascades, but it has been found to be both accurate and computationally efficient for the energy range of solar wind precipitation (Behrisch & Eckstein, 2007). Several surface properties have to be provided as an input and especially the optimal choice of often unconstrained surface binding energies that affect the sputtering process have been discussed recently (Szabo et al., 2020; Morrissey et al., 2022, 2023; Jäggi et al., 2023).

SDTrimSP-3D expands the SDTrimSP code to also take into account a three-dimensional surface geometry. This allows the simulation of slightly rough surfaces up to full porous regolith structures. As mentioned above, we have recently studied the role of regolith porosity on the total solar wind proton reflection with SDTrimSP-3D (Szabo, Poppe, et al., 2022). In this follow-up work, we examine more detailed properties of the backscattered solar wind H and compare it to observed ENA characteristics at the Moon. We

rely on the randomly generated regolith setups that were previously described in detail (Szabo, Poppe, et al., 2022) and use regolith inputs made up from 100 grains of the same size. The grain radius and simulation cell dimensions are determined in relation to the ion implantation depth (typically tens of nm for solar wind protons). Unless otherwise specified in the text, we use spherical grain shapes and a porosity of at least 80%, which showed the best agreement with measured ENA reflection coefficients. The porosity of the implemented regolith was typically between 80% and 85%. All regolith grains in our simulations are made up of enstatite $MgSiO_3$ with a density of 3.3 g/cm^3 . Simulations were performed using SDTrimSP-3D version 1.15, some simulations with flat surfaces were also performed with SDTrimSP 6.01, together with the graphical user interface described by Szabo, Weichselbaum, et al. (2022a), for cross-checking purposes.

SDTrimSP-3D does not track the charge state of incoming and outgoing projectiles as it lacks the physical capability of simulating the neutralization process. However, more than 95% of the reflected particles have become neutralized during backscattering from the lunar surface (Lue et al., 2018). As previously discussed, this only has a minor effect on interpretation of the results considering other uncertainties in the simulation (Szabo, Poppe, et al., 2022). We therefore neglect the charged component of the backscattered population and relate properties of all backscattered H from the SDTrimSP-3D simulations to ENA observations.

When comparing SDTrimSP-3D simulations to measured data, we set the solar zenith angle (SZA) as equal to the incidence angle on the regolith structure. This essentially approximates the Moon as a sphere that is covered by regolith, but otherwise smooth on global scales. Slopes due to the cratered landscape of the lunar surface are thus neglected, but their potential role is discussed later in the text.

3 Results for Simulated ENA Properties

3.1 ENA Scattering Angles

While first experimental observations had assumed isotropic ENA emission directions (Wieser et al., 2009), the full Chandrayaan-1 dataset allowed the construction of a scattering function describing the ENA emission directions under different SZAs (Schaufelberger et al., 2011; Vorburger et al., 2013). It was shown that the ENA emission shifts to a sunward-directed backward scattering under oblique incidence, as plotted in Figure 1 for SZAs between 60° and 75° (incident direction marked by the black lines). The grey area rep-

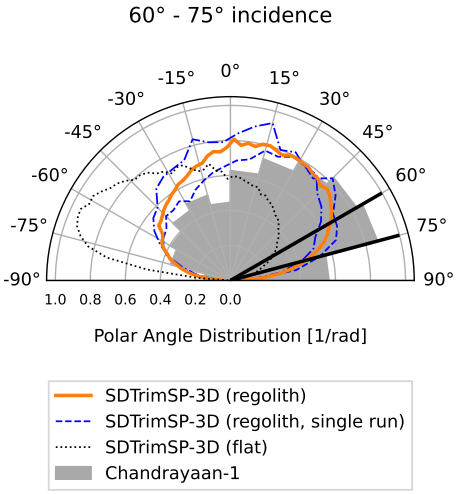

Figure 1. Polar angle distributions from SDTrimSP-3D show clear differences between the scattering behavior from a flat surface (dotted black line) and from the porous regolith (orange, compiled from five different regolith simulations). For the ion incidence between 60° and 75° (marked by the full black lines), significant forward scattering (negative angles) would be expected from a flat surface. However, the regolith surface shows a backward-dominated scattering behavior, which agrees with the Chandrayaan-1 observations of the ENA scattering function from the lunar surface (grey, from Schaufelberger et al. (2011)). The blue lines furthermore give two examples of single simulation runs at 70° incidence to illustrate that the scattering angles can vary for different regolith structures.

resents the polar angle distribution of emitted ENAs directly from Chandrayaan-1 measurements (Schaufelberger et al., 2011), with the relative uncertainty of the Chandrayaan-1 measurements being on average 4% (not shown). The angular distributions from the measurements were integrated over azimuth angles, while conserving information on forward scattering (polar angle $\theta < 0°$) and backward scattering (polar angle $\theta > 0°$). We follow the definition from Schaufelberger et al. (2011) of an azimuth angle of 0° representing the sunward direction. This leads to an integration over azimuth angle ranges of –90° to 90° for the backward component and over 90° to 270° for the forwards component. We apply the same integration to our simulation results and compare the Chandrayaan-1 data to SDTrimSP-3D simulations in Figure 1 for both a flat surface (black dotted line) and the regolith surfaces (orange). Regolith results shown here are compiled from simulations with five different randomly generated regolith structures, the relative standard deviation of these simulation results is between 5% and 20%. All simulations were performed with an energy spectrum of the incidence flux derived from the OMNI dataset (King & Papitashvili, 2005), averaged for the whole time span of the Chandrayaan-1 ENA measurements to correspond to the conditions of the data recording. This input flux has a mean energy of impacting solar wind protons of 750 eV and was used in the same manner in our previous study on total reflection coefficients (Szabo, Poppe, et al., 2022), where this is described in more detail.

The SDTrimSP-3D simulation shows that for an ideal flat surface, a significant forward scattering can be expected due to precipitating protons not being able to penetrate deep into the solid and therefore easily escaping the surface again. However, the opposite behavior develops when solar wind ions interact with a porous regolith. Our simulated ENA polar angle distributions have a pronounced backward-scattering that is in good agreement with the Chandrayaan-1 observations, clearly showing that observed scattering angles are closely related to the presence of regolith at the surface. The backscattering in the Chandrayaan-1 data appears even somewhat more prominent than predicted by our SDTrimSP-3D simulations. However, we found different random regolith structures produced backward scattering of different prominence, even though they were created with the same initial parameters and have almost the same porosities. This is illustrated by two examples for 70° given as the blue lines in Figure 1, showing that the angular scattering and the regolith structure are connected.

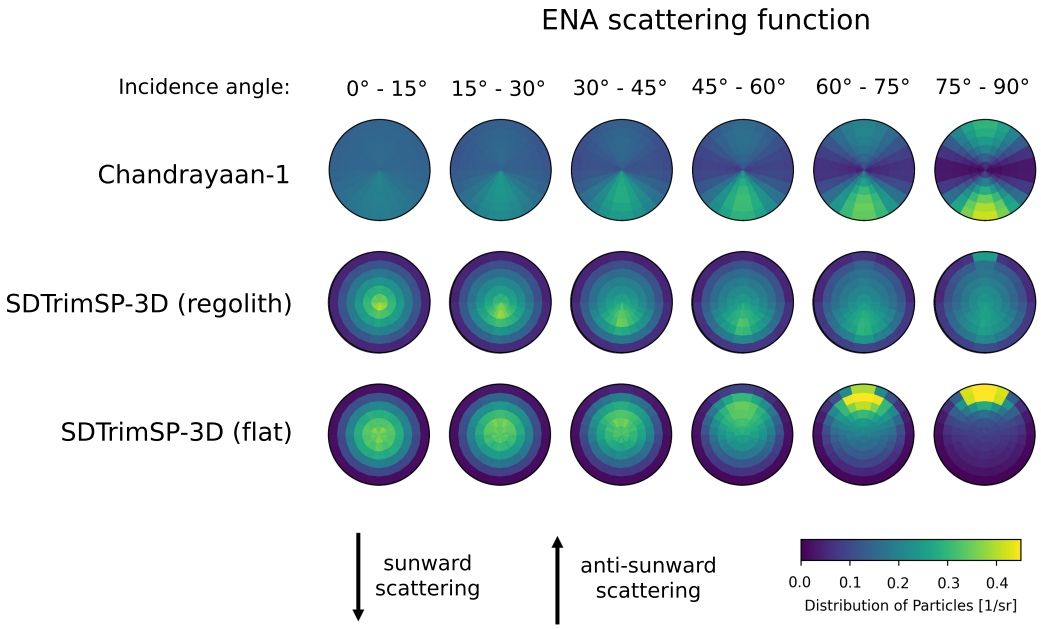

Figure 2. Full angular scattering functions from Chandrayaan-1 measurements in the first row, using the analytical fit from Vorburger et al. (2013), are compared to SDTrimSP-3D simulation results with regolith surfaces in the second row and with flat targets in the third row. The columns give different incidence angle ranges in 15° steps. Each of the maps is defined so that the center represents zenith direction, the distance from the center corresponds to the polar angle and the azimuth location in the circle corresponds to the azimuth scattering angle. The orientation is defined in the same manner as it was done by Schaufelberger et al. (2011), so that the downwards direction corresponds to sunward scattering and upwards to anti-sunward forward scattering.

We further compare our simulation results to the full scattering function derived from Chandrayaan-1 data in the form of polar maps in Figure 2, taking into account both polar and azimuth scattering angles. We again follow the convention used by Schaufelberger et al. (2011), plotting an azimuth angle of 0° (backward scattering) in the downward direction. The upward direction thus corresponds to forward scattering, as indicated by the arrows at the bottom of the figure. The first row of plots gives the analytical fit to Chandrayaan-1 measurements from Vorburger et al. (2013), the second row shows the results from SDTrimSP-3D regolith simulations and the bottom row represents simulations with a flat surface as a comparison. The columns indicate SZA ranges in 15° steps. The data in Figure 1 are the same as shown here, but integrated over azimuth angles to better depict total contributions of forward and backward scattering.

The scattering function derived from Chandrayaan-1 data in Figure 2 shows the extent of backward ENA emission towards the Sun as the main feature. For low SZAs close to normal incidence, the measured scattering function is largely isotropic and the backward scattering develops more strongly for higher SZAs. For oblique incidence, another smaller forwards scattering feature starts to develop as well. For the SDTrimSP-3D results, the polar maps demonstrate how the shift to more backward ENA emission for increasing SZAs is well captured in the regolith simulation, if generally somewhat broader in azimuth emission angle. The small forward-scattering contribution for large SZAs looks more pronounced in the measurements, but this feature is also more smeared out over azimuth angles in the simulation. In contrast, ENA emission for low SZAs is generally more isotropic in the measured data, while the simulated distributions show more of a concentration around the zenith direction. Comparison with the SDTrimSP simulation results with a flat surface shows the extent of the improvement from the regolith model. The flat surface does not cause any backward scattering, instead forward scattering completely dominates for higher SZAs.

We tested the sensitivity of the scattering function on regolith parameters by running one simulation with a lower porosity of around 0.5 and one simulation for irregular grain shapes, which were created with a fractal dimension $f_d = 2.6$ using an algorithm proposed by Wei et al. (2018) in the same manner as it was done in Szabo, Poppe, et al. (2022). Plots of these simulation results are given in the Supporting Information, but the differences to the high-porosity, spherical-grain case presented here are minor.

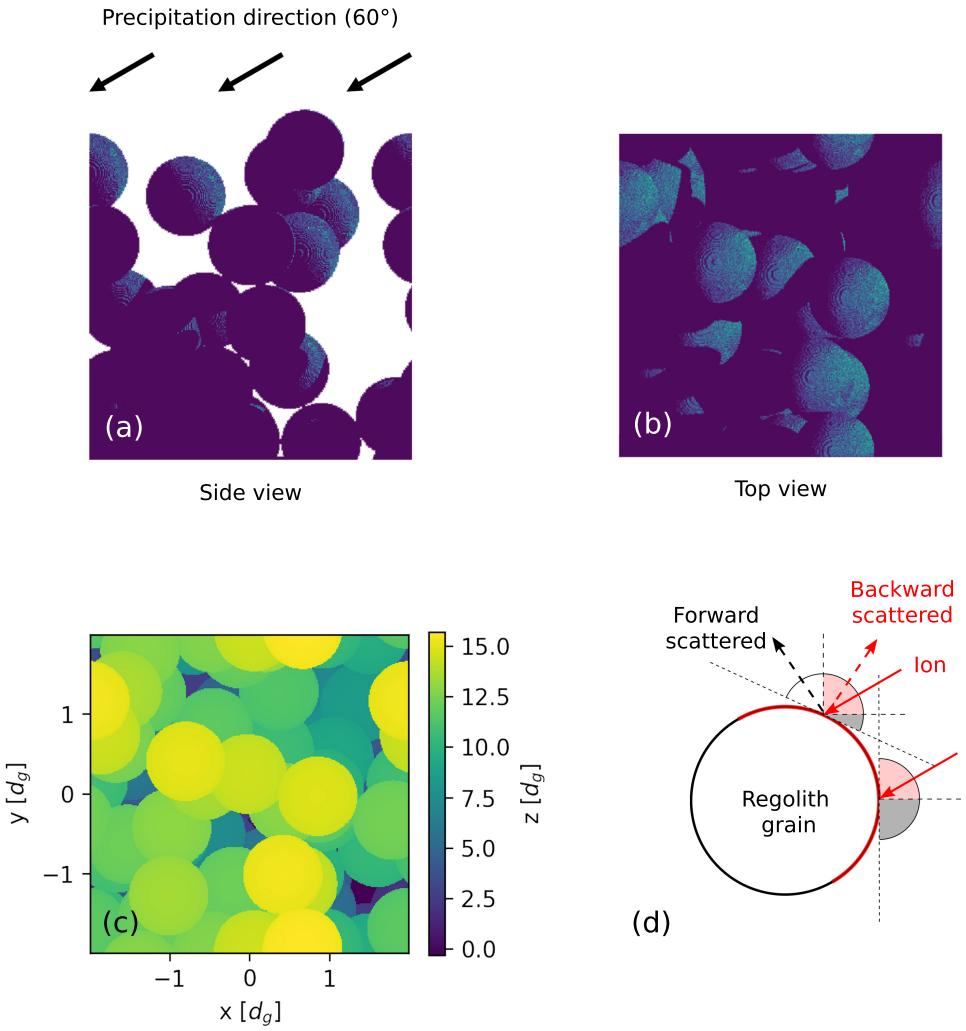

Figure 3. The role of the regolith geometry for ion precipitation and reflection is shown here, in a side view (a) and top view (b) of the first impact points on the surface. Proton precipitation occurs from the right at an incidence angle of 60° relative to the zenith direction. The plot in (c) also gives the height of the regolith grains in the top view, in units of the grain diameter d_g and in reference to the bottom of the simulation box. A clear preference of impacts on the right sunward-facing slopes of the grains is visible in panels (a) and (b). As sketched for a single grain in side view in panel (d), the solid angle where particle can theoretically be scattered into (semi-circles) is preferentially oriented towards the direction of incoming ions (red portion of semi-circles). Grey portions of the semi-circles denote scattering directions deeper into the regolith, from where escape is not possible without at least another scattering event. This geometry ultimately results in the backwards-favored ENA emission shown in Figures 1 and 2.

In relation to the sunward backscattered emission caused by the porous regolith geometry, Figure 3 shows the impact points on regolith grains for a 60° incidence from the right. Figures 3a and 3b give a side and top view respectively, while Figure 3c depicts the height profile, in reference to the bottom of the simulation box, as a reference for this example. Impact points on sun-facing parts of the regolith grains are evidently favored and from these locations on the grain, the backscattered particles are more likely to be emitted back into the direction of the precipitating ions. This is sketched in Figure 3d, showing a simplified scenario for ion incidence on a single spherical grain. Due to the oblique incidence direction, only the red-marked part of the grain can be impacted (assuming for this illustration no shadowing from other nearby grains). Depending on the impact point location, only certain scattering angles away from the grain are actually possible (marked by semi-circles). Initial downward scattering deeper into the regolith (grey area of the semi-circles) leads to certain scattering or absorption at other grains, while other solid angles could lead to escape from the regolith. However, due to the geometry of the impacts, these free solid angles are preferably oriented to the backward-scattered angles (red portion of semi-circles) rather than into forward-scattered angles. We also tested whether there are significant differences in how effective forward and backward scattering are from different depths below the top of the regolith. This could possibly explain a backward emission preference as well, but we didn't find this to be the case. Instead the combination of grain-geometry and the asymmetric incidence locations, leading to free solid angles that are also preferentially oriented towards the ion incident direction, stands out as the more significant source of backwards-favored ENA emission.

3.2 ENA Energies

Besides the scattering angle, the ENA energies represent a key aspect of ENA emission observations from the lunar surface. In the backscattering process, the narrow energies of the precipitating solar wind proton flux were measured to be significantly reduced and broadened upon reflection as ENAs from the surface. Futaana et al. (2012) characterized energy spectra of backscattered ENAs emitted near the lunar equator and close to zenith direction with a Maxwell-Boltzmann distribution. For differential ENA fluxes J_{ENA}, this was described as

$$J_{\mathrm{ENA}}(E) = \frac{R \cdot F_{\mathrm{SW}}}{2\pi} \frac{E}{(k_B T_{\mathrm{ENA}})^2} \exp\left(-\frac{E}{k_B T_{\mathrm{ENA}}}\right) \tag{1}$$

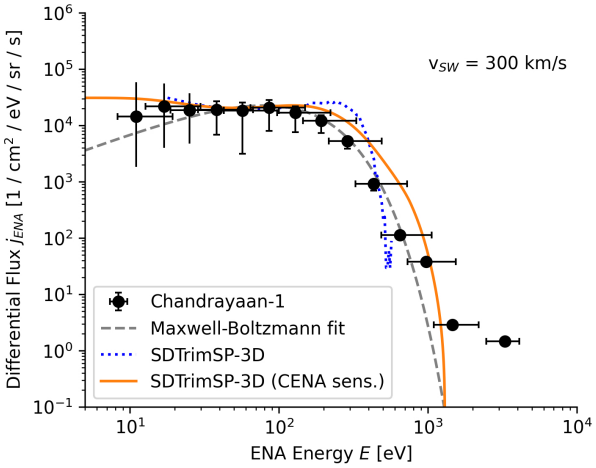

Figure 4. The energy dependence of the differential ENA fluxes at a solar wind velocity of 300 km/s is compared for measurements and simulations. The black points represent Chandrayaan-1 observations from Futaana et al. (2012) and the dashed grey line gives the accompanying Maxwell-Boltzmann fit. Error bar caps for the three measurement points at lowest energies have been omitted in this plot, indicating that calibration uncertainties represent an additional error source there (Futaana et al., 2012). Our regolith simulations (dotted blue line) produce slightly different energy spectra with a shoulder at higher energies compared to the measurements. Once the simulated sensitivity of the CENA instrument is considered (Kazama, 2006), a much improved agreement can be achieved (orange).

with the total reflection coefficient R, the solar wind flux F_{SW}, and the characteristic ENA energy $k_B T_{\mathrm{ENA}}$. Rather than a physical temperature, T_{ENA} is the characteristic parameter of the ENA energy spectrum that was found to linearly increase with the solar wind velocity (Futaana et al., 2012):

$$k_B T_{\mathrm{ENA}}[\mathrm{eV}] = v_{\mathrm{SW}}[\mathrm{km/s}] \times 0.273 - 1.99 \ . \tag{2}$$

In Figure 4, we provide an example comparison for the differential ENA flux as a function of energy from Chandrayaan-1 measurements to our simulation results. The experimental data (black markers) are taken from Figure 1 in Futaana et al. (2012), where CENA data from three consecutive Chandrayaan-1 orbits at different measurement ranges were combined to get a full energy spectrum. Solar wind parameter ranges for this measurement were reported as a density of 4.8 – 6.0 / cm^3, a velocity of 290 – 320 km/s and a temperature of 4.7 – 6.0 eV. The grey dashed line shows the Maxwell-Boltzmann fit from Equation 1, which nicely describes the energy spectrum of the measured ENAs.

For our SDTrimSP-3D regolith simulations, we chose a different input energy spectrum as in the previous section. Whereas the data collected for the study of the ENA scattering function were integrated over the entire mission (Schaufelberger et al., 2011; Vorburger et al., 2013), the Chandrayaan-1 ENA energy spectra from Futaana et al. (2012) were derived on a much shorter timescale. For the SDTrimSP-3D input energy spectrum, we thus use the differential flux of solar wind protons $J_{\mathrm{SW}}(E)$ impacting a surface normal to the flow direction, assuming a drifting Maxwellian velocity distribution with density n_0, drifting velocity $v_{\mathrm{SW}} = \sqrt{2E_{\mathrm{SW}}/m}$ and temperature T_{SW}:

$$J_{\mathrm{SW}}(E) = \frac{n}{2E_{\mathrm{SW}}} \cdot e^{-\frac{E+E_{\mathrm{SW}}}{k_B T_{\mathrm{SW}}}} \cdot \frac{1}{\sqrt{2\pi m k_B T_{\mathrm{SW}}}} \left[\left(1 - e^{\frac{2\sqrt{E \cdot E_{\mathrm{SW}}}}{k_B T_{\mathrm{SW}}}} \right) \cdot k_B T_{\mathrm{SW}} + 2e^{\frac{2\sqrt{E \cdot E_{\mathrm{SW}}}}{k_B T_{\mathrm{SW}}}} \sqrt{E \cdot E_{\mathrm{SW}}} \right] \tag{3}$$

For the temperature of the solar wind, we consider the spread of the incident energies, but not the incidence angles. More details on the derivation of Equation 3 and plots of the input energy spectra are given in the Supporting Information.

The dotted blue line in Figure 4 shows the energy dependence of the simulated differential ENA flux for the average conditions of the Chandrayaan-1 example of $n_0 = 5.4$ / cm^3, $v_{\mathrm{SW}} = 300$ km/s and $T_{\mathrm{SW}} = 5$ eV at a SZA of 0°. For this evaluation, we only selected ENAs emitted within 20° around the zenith direction. This was chosen to be in accordance with the measurement selection criteria by Futaana et al. (2012), who only used cases where the viewing direction and the zenith location were at most 10° off and stated their angular resolution as 6.5° × 45°. Directly from this evaluation of simulation results (blue), we get an almost constant differential ENA flux at lower energies with a shoulder and a steep drop-off at around 300 eV. The Chandrayaan-1 energy spectrum is generally well reproduced, but the shoulder before the drop-off occurs more abruptly at somewhat higher energies in the model results.

However, it has to be considered that the CENA instrument has a limited energy resolution of $\Delta E/E \approx 100\%$, which was shown by Hodges (2011) to affect the shape of the ENA energy spectrum. Kazama (2006) give energy calibration curves for three different energies from simulations of their instrument geometry, showing the energies that are measured by the CENA instrument (see also Kazama et al. (2007)). Saito et al. (2021) confirmed $\Delta E/E = 100\%$ for H in further experimental calibration studies

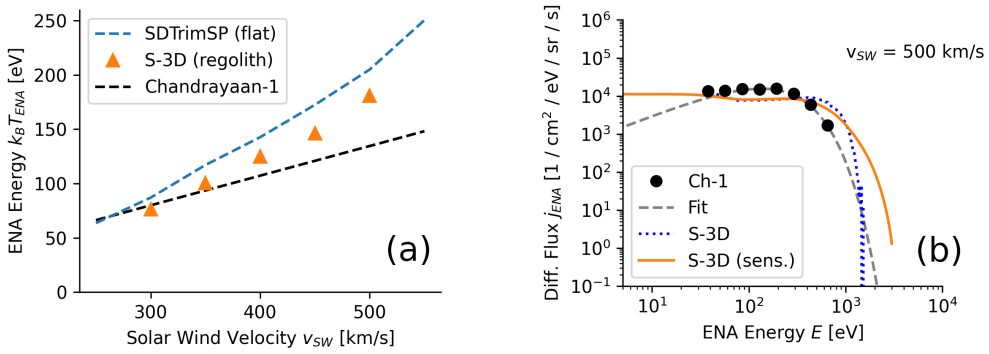

Figure 5. (a) Futaana et al. (2012) found a linear increase of the characteristic ENA energy with solar wind velocity (black). A similar increase is observed in the SDTrimSP-3D regolith model "S-3D", orange), but the increase is steeper than in the measurements and ENA energies are overestimated in the simulation for fast solar wind velocities. The simulated characteristic ENA energies are furthermore not significantly dependent on the regolith structure, as simulations with flat surfaces produce very similar results (blue).
(b) The detailed comparison of energy spectra for a solar wind velocity of 500 km/s from Chandrayaan-1 measurements ("Ch-1", black) and SDTrimSP-3D simulations are shown here. With the CENA sensitivity, the shape of the measured spectra looks similar (orange), but the energy of the drop-off is overestimated.

for the ENA instrument of the BepiColombo MMO orbiter, which is a replica of the CENA instrument (Saito et al., 2010). Based on the simulated calibration curves by Kazama (2006), we estimated instrument sensitivity curves for all measurement energies in a likely similar manner as was done by Hodges (2011). We achieved this by normalizing the curves from Kazama (2006) by their nominal energy and linearly interpolating between them (see the Supporting Information for more details). We convolve our results from SDTrimSP-3D with these calibration curves to derive a model of the actual measurement of the CENA instrument. This result is included in Figure 4 as the solid orange line and it follows the actual experimental observation excellently in both absolute value of the differential ENA flux and decrease with higher ENA energies. The SDTrimSP-3D regolith model even works better than the Maxwellian fit in describing the constant flux below about 100 eV.

We performed SDTrimSP-3D simulations at various solar wind velocities to test the observed correlation of this parameter with the characteristic ENA energies. To account for the correlation of solar wind velocity and temperature (Lopez & Freeman, 1986), we analyzed solar wind parameters from the OMNI dataset for the CENA operation time between January 2009 and July 2009 (King & Papitashvili, 2005). The median solar wind temperature at a given solar wind velocity corresponded close to the linear fit of

$$k_B T_{\mathrm{SW}}[\mathrm{eV}] = 0.0449 \times v_{\mathrm{SW}}[\mathrm{km/s}] - 11.98 \,. \tag{4}$$

An overview of the OMNI data is given in the Supporting Information. Ultimately, the solar wind temperature was not found to play a significant role for our simulation outcomes. This is in line with the observations from Futaana et al. (2012), where a weak correlation between the solar wind temperature T_{SW} and the characteristic ENA energy $k_B T_{\mathrm{ENA}}$ was reported, but attributed to the correlation of T_{SW} and v_{SW}.

Figure 5a shows the results for the characteristic ENA energy from our simulations at different solar wind velocities, compared to the linear fit of Equation 2 to the measured data (Futaana et al., 2012). As described previously, $k_B T_{\mathrm{ENA}}$ was chosen as a characteristic parameter due to the Maxwell-Boltzmann fit to the measured ENA energy spectra. Our simulation results are not as well described by such a fit, but we can calculate an equivalent $k_B T_{\mathrm{ENA}}$ from the mean energy $\langle E_{\mathrm{ENA}} \rangle$ of the modeled ENA spectra. The Maxwell-Boltzmann distribution from Futaana et al. (2012) gives $\langle E_{\mathrm{ENA}} \rangle = 3/2 \; k_B T_{\mathrm{ENA}}$. We thus derive $k_B T_{\mathrm{ENA}}$ for our SDTrimSP-3D simulations by converting the differential flux to a distribution function, calculating the mean ENA energy $\langle E_{\mathrm{ENA}} \rangle$ from integration and multiplying the result by 2/3.

As shown in Figure 5a, we achieve a very good agreement between the regolith simulations (orange) and the experimental fit (black) for low solar wind velocity, as expected from the well-fitting comparison of the spectra shown in Figure 4. However, the experimental and simulated curves slightly drift apart for higher solar wind velocity v_{SW}, with the simulations consistently overestimating the observed ENA energies. Figure 5b gives the detailed comparison for an example of $v_{\mathrm{SW}} = 500$ km/s. The shape of the energy spectrum of the differential ENA flux looks similar for measurement and SDTrimSP-3D simulation, but the high energy tail extends further in the simulations.

Figure 5a also compares simulation results for the characteristic ENA energy from regolith simulations (orange) and simulations with a flat surface (blue), which only show slight differences. Similarly, the ENA energies were also not found to depend significantly on the SZA and thus the incident direction. For the 300 km/s case, we found a small $k_B T_{\mathrm{ENA}}$ increase from 76 eV at 0° to 79 eV at 60°, for 500 km/s the increase is from 181 eV to 198 eV, which has a similar small trend as observed by Vorburger et al. (2016). The plots in Figures 4 and 5 are ultimately all given for 0°.

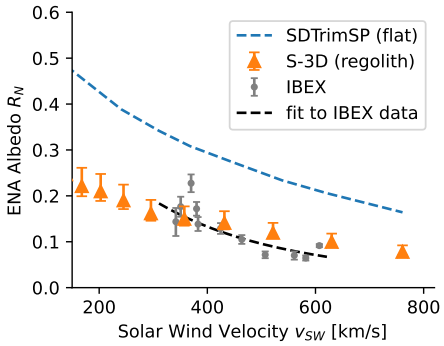

Figure 6. The global lunar ENA albedo R_N as calculated from the SDTrimSP-3D regolith model (orange) is compared to IBEX data from Funsten et al. (2013) (grey, fit in black). ENA albedos from a simulation with a flat surface are included as well (blue). In general, the ENA albedo decreases for faster ion impacts as the ions penetrate deeper below the surface and are less likely to be reflected. However, the absolute values of the albedo reported from IBEX can only be explained by considering the presence of highly porous regolith.

3.3 Energy Dependence of the Reflection Coefficient

From our simulations at different energies, we can also study the possible solar wind velocity dependence of the total reflection coefficient, where varying reports exist. Funsten et al. (2013) showed a slight decrease of the reflection coefficient for higher proton impact energies in their IBEX data analysis, which can generally be expected due to faster ions being able to reach deeper into the solid and reflection becoming more unlikely. The extent of the decrease was observed from about 0.2 to 0.07 over the whole range of observed solar wind velocities. Futaana et al. (2012) originally had not reported a significant correlation in the CENA data, but this could be related to statistical scatter in their data. Lue et al. (2018) did observe a decrease of the proton scattering efficiency as well, but here it is unsure whether the unknown neutralization probability in interatomic collisions could affect these results.

In Figure 6, we compare SDTrimSP-3D simulation results for the global ENA albedo (orange), i.e., the reflection coefficient averaged over all incidence SZAs weighted by the cosine of the SZA, with the IBEX data from Funsten et al. (2013). For this purpose, we performed SDTrimSP-3D regolith simulations at ten logarithmically spaced energies between 100 eV and 3 keV and incidence angles between 0° and 80° at steps of 20°. Here, incident protons at each solar wind speed were modeled as mono-energetic beams, i.e., we neglected the solar wind temperature due to its relatively minor effect on the over-

all emission albedo. Funsten et al. (2013) determined global lunar ENA albedos R_N at different solar wind velocities by assuming the reflection coefficient to be independent of the angle. Their derived values (grey points in Figure 6) could be fitted by $R_N = 1/(2.3+ 6.3\times E$ [keV]) (black dashed line). As evident in Figure 6, there is a very good agreement between the prediction of our SDTrimSP-3D regolith model (orange triangles, error bars calculated in the same manner as in Szabo, Poppe, et al. (2022)) and the behavior observed by IBEX. The simulations suggest ENA albedos of around 0.2 at a solar wind velocity v_{SW} of 200 km/s decreasing down to around 0.1 for 600 km/s. We also include simulations from a flat surface (blue), which correspond to assuming the Moon to be a smooth sphere. These results show a similar decrease with increasing solar wind velocity, but significantly overestimate the ENA albedo. This provides further evidence for the importance of considering the regolith in the ion-surface interaction and represents an additional verification of our SDTrimSP-3D regolith model.

4 Discussion of Backscattered ENA Properties

Based on a detailed model of the interaction between an impinging solar wind proton and a set of stacked regolith grains, we have studied the solar wind backscattering process to model observations of the ENA emission from the surface. After previously demonstrating that the regolith porosity plays a key role in the solar wind proton reflection and can be constrained from ENA measurements (Szabo, Poppe, et al., 2022), the ENA characteristics such as the emission angles and energies have now been investigated.

4.1 Scattering Angles

For the ENA scattering angles, our SDTrimSP-3D regolith model reproduces the main features of the scattering function from Chandrayaan-1 observations, which observed sunward backscattering under increased SZA (Schaufelberger et al., 2011). The same behavior is observed for the regolith simulations and can be connected to a geometry-related impact point favoring on the sunward-facing slopes of the regolith grains, from which scattering back into the incident direction becomes more likely. Due to this effect, the otherwise significantly forward-oriented emission of scattered H on a flat surface (Niehus et al., 1993) is shifted into a distribution that peaks sunward close to where solar wind protons impact from. This has been proposed already when those anisotropies were first reported (Schaufelberger et al., 2011). It is also in line with the porous regolith structure

contributing significantly to backwards-favored light scattering that can even cause an opposition effect surge from the surfaces of the Moon and other planetary bodies (Helfenstein et al., 1997; Hapke et al., 1998). This result further supports that the regolith structure plays a key role in the plasma-surface interaction on any planetary body and should be considered for ENA emission from reflected ions and all other related phenomena such as implantation or sputtering by ion impact.

Some details in the scattering function show discrepancies between measurement and simulation; in particular the measured distributions are more isotropic for small SZAs, while the forward and backward scattering peaks are more focused for larger SZAs. The highest SZAs show an almost complete lack of side scattering in the observations, while this does not occur in the simulations. In the same manner as the porosity affects the total reflection of solar wind protons, the detailed appearance of the scattering function can possibly be related to further regolith properties. The main simulations presented here were performed with spherical regolith grains of the same size, which evidently contains several approximations. As mentioned above, we calculated the distribution of ENA scattering angles using non-spherical grains with a fractal dimension of $f_d = 2.6$ created following the algorithm by Wei et al. (2018) (see Szabo, Poppe, et al. (2022) for more details). This showed overall very similar results, and in particular, the isotropy of scattering under small SZAs could not be explained in this manner. However, these grain shapes possibly don't represent enough deviation from a spherical shape to encapsulate all aspects of ions impacting irregular grains. Therefore, further modeling studies with more detailed grain shapes, small-scale roughness, and grain-size distributions should be undertaken. This could give important insights whether ENA scattering function aspects beyond the favored backward emission can be explained. For our simulations, some randomly created regolith setups showed more backward scattering than others, indicating that some aspects of the regolith structure are also imprinted in the scattering function. For our simulated regolith setups, differences in the grain order at the top are likely the reason for these variations, but further, more detailed simulations should be done to derive a quantitative relation. Again, further grain shapes could provide essential insights as they will affect the near-surface impacts (Kulchitsky et al., 2018) and the free solid angle for backscattering. Overall, the scattering function could be helpful for constraining further regolith properties in the future. On top of that, future work should also consider the effect of larger scale roughness and slopes as suggested by Schaufelberger et al.

(2011). In this context, it would also be of interest to test whether the whole regolith-covered surface can be approximated by a conventional rough surface. Defining characteristic roughness parameters for the backscattering behavior, which has similarly been proposed for sputtering of rough surfaces by ion impacts (Cupak et al., 2021; Szabo, Cupak, et al., 2022), could be helpful for describing the ion interaction with regolith on planetary bodies. In the same manner, scattering laboratory experiments for planetary surface analogs or even returned lunar samples should be conducted to constrain possible uncertainties in the hydrogen scattering behavior predicted by SDTrimSP.

4.2 Scattering Energies and Reflection Coefficients at Different Solar Wind Velocities

Besides the scattering angles, we also analyzed the emission energies of backscattered ENAs from our SDTrimSP-3D regolith simulations and compared them to measurements from the Chandrayaan-1 CENA instrument. Our calculations reproduce the broad ENA spectra reported from Chandrayaan-1 (Wieser et al., 2009; Futaana et al., 2012) and IBEX (Rodriguez M. et al., 2012; Allegrini et al., 2013). For the more common slow solar wind configurations, we achieve an excellent agreement between the model and the satellite measurements, once the CENA instrument sensitivity is considered. The latter aspect agrees with the finding by Hodges (2011) and indicates that CENA's broad energy acceptance smears out the drop-off in the spectrum near the maximum scattering energies. In contrast to the model from Hodges (2011), our calculations are also consistent with observations in regards to the total reflection probability and thus the absolute value of the ENA flux, similar to the MD model by Leblanc et al. (2023). However, our simulated energy spectra fit the lunar observations better than the MD results, which we mostly attribute to the electronic energy loss that is included in the SDTrimSP-3D calculations (Correa, 2018; Mutzke et al., 2019). The electronic stopping represents the major source of energy loss for protons at the typical solar wind energies - for the example of 300 km/s proton impacts on a flat surface, SDTrimSP attributes about 65% of the total energy loss to electronic stopping. This effect thus plays an important role in describing the ion-surface interaction and should be considered for modeling ENA emission energies.

We performed simulations at various solar wind velocities v_{SW} and confirmed that this parameter is the main driver of the ENA energies, especially for the ENAs emitted

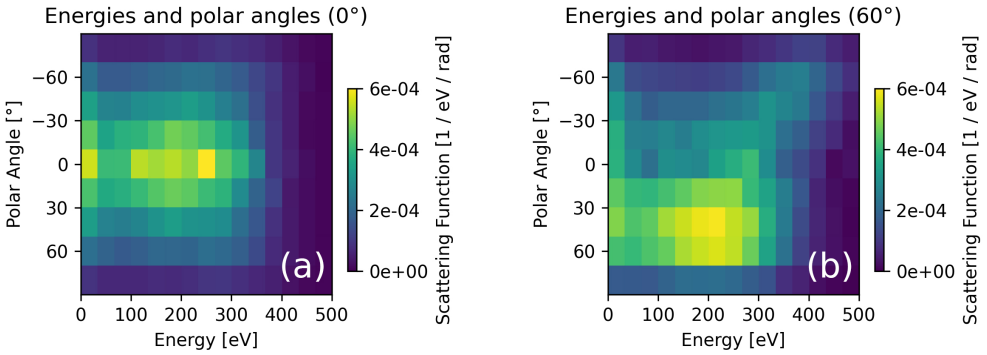

Figure 7. Scattering functions at different energies and polar angles are depicted here for (a) 0° and (b) 60° incidence at a solar wind velocity of 300 km/s, corresponding to close to 500 eV. In the same way as for Figure 1, the scattering function was integrated over azimuth angles while keeping the distinction between forward scattering (negative polar angles) and backward scattering (positive polar angles) intact. These plots show that ENAs are emitted at broad energies and angles, but those parameters do have some correlation. While backward emission is dominant for the 60° case, the high energy ENA population ($E \gtrapprox 300$ eV) shows a preferential forward scattering.

close to the zenith direction as chosen in the analysis of Futaana et al. (2012). The solar wind velocity also affects the total reflection coefficient and our model reproduces IBEX measurements for the global ENA albedo, which can be expected to decrease from around 0.2 at slow solar wind velocities to somewhat below 0.1 for the faster solar wind. Simulations at different incidence angles show only a minor effect on the simulated characteristic ENA energies, consistent with the slight increase for higher SZAs reported by Vorburger et al. (2016). For oblique incidence, the total scattering angle between the precipitation direction and the outgoing direction for achieving reflection from the surface can be smaller than for normal incidence. Such a smaller change of momentum direction tends to be connected to smaller energy transfer in interatomic collisions. This aspect also causes scattering angles and energies to be correlated, as shown in the energy-polar-angle maps in Figure 7. Simulation results for a solar wind velocity of 300 km/s are depicted under normal incidence (0°) in Figure 7a and 60° in Figure 7b. Similar to Figure 1, positive polar angles denote backward scattering while negative polar angles give the forward scattering contribution. The 60° plot shows the dominant contribution of the backward scattering at energies below around 350 eV, as well as a tail of forward scattering projectiles that appears at energies above 300 - 350 eV. Such a correlation be-

tween scattering energies and angles should be kept in mind for future analysis of backscattered ENAs from planetary surfaces.

For the energies of ENAs emitted around the zenith direction, only small differences between SDTrimSP-3D simulations for a flat surface and a regolith surface could be found. Instead, the energies of these ENAs are mostly determined by the energies of the precipitating solar wind protons. Our simulations thus support that this evaluation regime is well suited to use ENAs for studying surface precipitation. While knowledge of the surface-structure-dependent total reflection coefficient is important to predict the correct total ENA flux, the ENA energy spectrum can be directly connected to the incident energies. However, with the application of backscattered particles for laboratory analysis in mind, the surface composition can be expected to affect the energy spectra of ENAs as well. The LEIS sample analysis method uses this to identify surface composition from the energy spectrum of backscattered ions (Niehus et al., 1993). We will investigate the extent of this effect on ENA emission from planetary bodies in the future.

For higher solar wind velocities, an increasing offset between modeled and measured ENA energies does exist and our simulations overestimate the ENA energies compared to the measurement. Similarly, comparison of the global lunar ENA albedo shows that SDTrimSP-3D predictions are slightly higher than IBEX measurements for faster solar wind velocities, even though this is only a minor offset. This could potentially be explained by a general underestimation of the energy loss in SDTrimSP-3D at these conditions. As mentioned before, the regolith itself only has a small effect on simulated ENA energies, at least when ENAs emitted around the zenith direction are considered. Therefore, it seems unlikely that approximations in the regolith implementation are the cause for this offset. Instead there might be some improvement necessary for how SDTrimSP fundamentally calculates the interaction and energy loss of a proton that impacts a silicate surface. As discussed in our previous study (Szabo, Poppe, et al., 2022), laboratory experiments would be helpful to constrain SDTrimSP input parameters, mainly the electronic stopping that controls the energy loss due to electron interactions. At typical solar wind energies, this represents an important energy loss mechanism as was discussed above. Contrary to the nuclear stopping from interatomic collisions, the BCA applied in SDTrimSP does not allow the direct calculation of the electronic stopping. Instead, tabulated values and empirical models are used and the electronic stopping power for

compounds is typically calculated as a weighted average from values for its elemental constituents (Behrisch & Eckstein, 2007; Mutzke et al., 2019). This has been shown to be of limited accuracy for oxides (Roth et al., 2017), however, an overestimation of the electronic energy loss in the weighted-average approach was found. Similarly, proton implantation experiments with olivine samples at 10 and 20 keV (Bissbort et al., 2023) indicate that the stopping power is generally slightly overestimated. Therefore, this does not appear to offer an explanation for the evident underestimation of the proton energy loss. We tested increasing the electronic stopping in SDTrimSP by a constant factor (using the `ck_elec` parameter of SDTrimSP). For an electronic stopping power increase by a factor of 2, the average ENA energy is brought to better agreement with the CENA data for 500 km/s, but then the comparison with data at lower velocities is off. Generally, BCA codes like SDTrimSP should be well-suited for modeling measured backscattering energy spectra (Goebl et al., 2013; Tran et al., 2019; Shams-Latifi et al., 2022). With the existing literature only suggesting a correction in the opposite direction than what would be needed to explain our offsets, the stopping power therefore does not provide an obvious solution for the discrepancy between SDTrimSP simulations and CENA data.

Solar wind protons that are reflected as protons have been shown to have significantly higher energies as the backscattered neutrals, as is detailed in the extensive analysis by Lue et al. (2018). Because of a certain neutralization probability during each interatomic collision (Beikler & Taglauer, 2001; Hodges, 2011), this can be expected due to reflected protons having systematically fewer collisions and thus a smaller energy loss. This could in theory play a role for our simulation results as the SDTrimSP code is not able to track the projectile charge state. However, Lue et al. (2018) have also shown that the scattering efficiency as a proton is consistently lower than 1%. Protons can thus be expected to only make up a few percent of all backscattered H and their contribution is far too low to account for the offset in the ENA scattering energy.

On the other hand, both our simulations as well as the earlier work by Hodges (2011) demonstrate that the energy resolution of the CENA instrument at $\Delta E/E \approx 1$ does play a role in the interpretation of the ENA spectra. Wang et al. (2021) have performed analysis of ENAs measured by the Chang'E-4 mission and overall find a similar relation between characteristic ENA energy and solar wind velocity as Futaana et al. (2012). Funsten et al. (2013) do report a systematic underestimation of IBEX ENA counts by the empirical fit from Futaana et al. (2012) at high ENA energies. However, the apparent cor-

relation between scattering angles and energies should be taken into account and this discrepancy might as well be related to the significantly different viewing geometries of the IBEX and Chandrayaan-1 missions. Overall, these considerations do not give an immediate explanation for the offset between experiment and simulation either. As discussed before, further simulations and laboratory experiments of the proton scattering process should be undertaken to allow for an improved theoretical description of ENA emission at fast solar wind velocities.

5 ENA Emission from the Moon and Mercury

5.1 Test-Particle Model

Using the scattering functions from SDTrimSP-3D that describe energies and angles of reflected H, the H ENA fluxes measured in the orbits around the Moon and Mercury can be estimated when the precipitation fluxes are considered. To do so, we apply a Monte Carlo model to compute ENA fluxes in a similar manner as it is regularly done for exosphere modeling (Tucker et al., 2019; Killen et al., 2022). Due to the comparably high ENA energies, we can neglect any gravitational effects, and use a straight-line approximation for the ENAs traveling through three-dimensional space. The coordinate system is chosen such that the origin is in the center of the planetary body, the x-axis points towards the Sun, the z-axis points north normal to the ecliptic plane and the y-axis completes the right-handed set. For this purpose, we ran a range of SDTrimSP-3D simulations at different incident energies and angles as a base dataset to model solar wind proton scattering from the surfaces of the Moon and Mercury. Input distribution functions were averaged over the azimuth direction while conserving information of forward and backward scattering. This gives scattering functions $f_S(E_{\mathrm{in}}, \theta_{\mathrm{in}}; E_{\mathrm{out}}, \theta_{\mathrm{out}})$ depending on polar angles θ and energies E of both precipitating protons ("in") and scattered H ("out") in the same form as the examples shown in Figure 7. The normalization was chosen in a manner such that the integral corresponds to the total reflection probability $R(E_{\mathrm{in}}, \theta_{\mathrm{in}})$ from the specific SDTrimSP-3D simulation:

$$\int_{-\pi/2}^{\pi/2} \int_{0}^{\infty} f_S(E_{\mathrm{in}}, \theta_{\mathrm{in}}; E_{\mathrm{out}}, \theta_{\mathrm{out}}) \cdot \sin(\theta_{\mathrm{out}}) \; dE_{\mathrm{out}} \; d\theta_{\mathrm{out}} = R(E_{\mathrm{in}}, \theta_{\mathrm{in}}). \tag{5}$$

As discussed previously, R only increases very slowly with incidence angle θ_{in} due to the highly porous regolith structure (Vorburger et al., 2013; Szabo, Poppe, et al., 2022), while it slightly decreases with increasing energy E_{in} (see Figure 6).

Total ENA fluxes are calculated by tracing a large number of test particles (typically $> 10^6$ ENAs per simulation) emitted from the surface at positions according to the precipitation of solar wind protons to the planetary surface (see details in Sections 5.2 and 5.3 below for the Moon and Mercury, respectively). Initial ENA speeds are randomly chosen with a uniform distribution up to the maximum energy of each precipitating proton, while the initial ENA angles are uniformly chosen over the full 2π solid angle oriented away from the surface. Each test particle is then assigned a flux according to the precipitation flux at the location of origin and the scattering probability for the chosen emission energy and angles according to the SDTrimSP-3D scattering functions. Model ENAs are tracked until they reach an outer boundary of 5 planetary radii and local densities and fluxes are recorded in a three-dimensional Cartesian array for later analysis.

5.2 ENA Fluxes at the Moon

For the scenario of the Moon upstream of Earth's bow shock, the precipitating solar wind flux decreases with the cosine of the solar zenith angle, but otherwise impacts the surface constantly to a good approximation (i.e., neglecting the effects of lunar crustal magnetic fields (Vorburger et al., 2012; Futaana et al., 2013)). Figure 8a shows the ENA fluxes in the xz-plane around the Moon relative to the solar wind flux. The solar wind upstream parameters of a density of 5 / cm^3 and a solar wind velocity of 400 km/s were chosen, corresponding to a solar wind flux of 2×10^{12} / m^2 / s. A broad, but primarily sunward-peaking ENA flux distribution can be observed and only small ENA fluxes downstream of the Moon from forward scattering near the terminator are predicted. These features are evidently related to the dayside precipitation of the lunar surface (see 8b) together with the preferential sunward backscattering of ENAs due to the regolith geometry. This is the same picture that has been reported for the Chandrayaan-1 observations in the form of decreasing ENA emission from higher latitudes (Wieser et al., 2009). ENA emission from locations up to 30° beyond the terminator on the nightside does occur as seen by Chandrayaan-1, likely due to solar wind plasma being transported to the nightside (Vorburger et al., 2016). Small ENA fluxes can thus also be expected in the

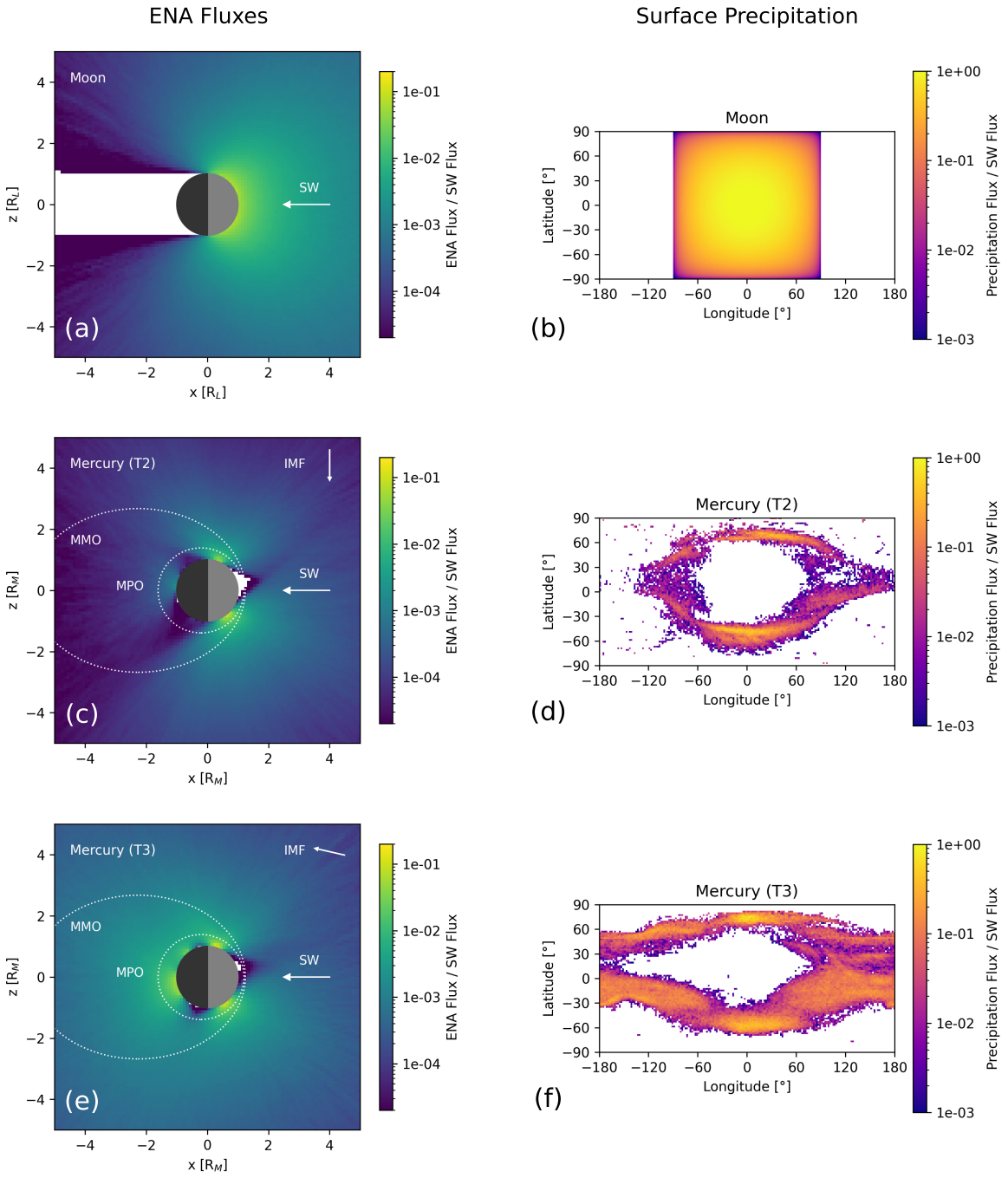

Figure 8. Simulated ENA fluxes (a, c, e) and surface precipitation maps (b, d, f) are shown for the Moon and Mercury. For the Moon in the solar wind, a parallel solar wind with a flux of 2×10^{12} / m^2 / s was assumed. The Mercury plots are based on precipitation inputs from the T2 (southward IMF) and T3 (planet- and northward IMF) cases of hybrid plasma modeling from Fatemi et al. (2020) with a solar wind flux of 1.1×10^{13} / m^2 / s. Clear differences in the ENA scenarios at the Moon and Mercury can be observed, with the latter being driven by variable precipitation due to Mercury's highly variable magnetosphere. Our model results show that the magnetospheric response to solar wind upstream conditions is mirrored in the ENA environment around Mercury. At lower altitudes, MPO and MMO will be able to observe ENA emission with relatively high spatial resolution, while especially MMO measurements at larger distances should give insights into ENA emission on a global scale.

ENA-wake sketched in Figure 8a (white area, representing a non-existent flux) even when the Moon is outside of Earth's bow-shock; however, such effects are not captured here in our simulations that assume only dayside precipitation. As mentioned above, further effects can also be expected by the presence of lunar crustal fields, leading to reduced surface precipitation and similarly reduced ENA emission especially at the South Pole-Aitken basin (Lue et al., 2011; Vorburger et al., 2015).

5.3 ENA Fluxes at Mercury

In contrast to the Moon, surface precipitation and ENA emission at Mercury become much more complex and require a full plasma model to account for the relevant charged-particle fluxes and electromagnetic fields (Benna et al., 2010; Pfleger et al., 2015; Varela et al., 2015; Fatemi et al., 2020). For the ENA emission, Lue et al. (2017) presented predictions from Mercury's surface based on empirical formulas for the lunar observations, suggesting high ENA fluxes from proton backscattering and broad energy spectra. Leblanc et al. (2023) also estimated H ENA fluxes from the surface of Mercury by combining scattering simulations with a hybrid plasma model result.

In order to study the effect of proton precipitation properties on the emitted ENA flux at Mercury, we take the surface precipitation results from the plasma simulations from Fatemi et al. (2020). Fatemi et al. (2020) performed hybrid modeling for several solar wind upstream conditions to illustrate precipitation at the polar cusps and Mercury's nightside as well as their variability in regard to different solar wind and IMF conditions. In particular, we include surface precipitation maps from their T2 and T3 cases as an input and calculate the resulting ENA fluxes using the test-particle model used in the previous section. Both simulation cases describe a solar wind with a density of 30 / cm^3, a velocity of 370 km/s and an IMF strength of 18 nT. The solar wind flux in these examples is thus 1.11×10^{13} / m^2 / s. The two cases only differ in IMF direction: T2 represents an idealized case of a purely southward-pointing IMF, while the T3 simulation considers an IMF that is primarily planetward directed (17.55 nT) with a small component (4 nT) northward, similar to one of the MESSENGER flyby cases also discussed in Fatemi et al. (2020). For the input of ENA emission angles and energies, we use SDTrimSP-3D results at ten proton incidence energies between 100 eV and 3000 keV and 20° incidence-angle steps, which was also the basis for calculating lunar ENA albe-

dos in section 3.3. In doing so, we assume the same porosity and generally the same regolith scattering behavior as for the lunar surface.

Figures 8c and 8e then give the ENA fluxes around Mercury from our model. As predicted by the hybrid plasma simulations, the main precipitation generally occurs in polar cusps at high dayside latitudes and in low nightside latitudes, which is plotted in Figures 8d and 8f for southward IMF (T2) and mostly planetward IMF (T3). However, the extent of the precipitation for these features varies significantly for different IMF conditions. In particular, nightside ion impacts are much more common and more broadly distributed for the T3 case than for T2. Fatemi et al. (2020) discuss that this could be caused by increased precipitation from quasi-trapped proton populations. For the planet- and northward IMF corresponding to the T3 case, Schriver et al. (2011) reported MESSENGER observations of quasi-trapped ions above Mercury's nightside. Hybrid models by Herčík et al. (2016) have also shown that these IMF conditions are favorable for larger populations of quasi-trapped ions. As the ENA emission by backscattering is driven by the precipitation, this behavior is directly translated into the modeled ENA fluxes observed around Mercury. The increased proton fluxes impacting Mercury's nightside in the T3 simulation cause a significantly higher nightside ENA response than for the T2 case with southward IMF component. Some increase also shows up in ENA fluxes above the polar cusps, where the larger area that is impacted by protons causes high ENA fluxes to extend further out in the T3 case. This clearly demonstrates the significant response of ENA fluxes to changing precipitation conditions and provides further evidence that ENA measurements will be very well suited to derive surface precipitation.

BepiColombo will observe ENAs around Mercury with both of its modules and variations in ENA fluxes as sketched in Figures 8c and 8e. The magnitudes of the ENA fluxes are around 10^9 to 10^{12} /m^2/s (10^{-4} to 10^{-1} of the solar wind flux) depending on the exact location and distance from Mercury. The scenario sketched by our model coincides with the outcomes predicted by Lue et al. (2017), who suggested emission from polar cusps up to 10^{12} /m^2/s accompanied by somewhat weaker dayside and nightside ENA emission. Leblanc et al. (2023) generally predict lower fluxes observed by BepiColombo than our study, but this can mostly be attributed to differences in the inputs from hybrid model results. The precipitating surface fluxes stated by Leblanc et al. (2023) only go up to about 3×10^{11} /m^2/s, while Fatemi et al. (2020) predict local surface precipitation on

the order of 10^{12} /m^2/s, which is consistent with other hybrid model predictions from Kallio and Janhunen (2003) and Pfleger et al. (2015).

In any manner, the ENA environment around Mercury can be expected to be readily observable with either ENA instruments on MPO and MMO (Orsini et al., 2021; Saito et al., 2021). With polar orbits of 480 × 1500 km ($0.20 \times 0.61 R_M$) and 590 × 11640 km ($0.24 \times 4.77 R_M$) (Benkhoff et al., 2021), the MPO and MMO spacecraft will cover a wide range of distances from Mercury. As a result, they will also be able to probe several ENA flux regions. Figures 8c and 8e illustrate that this represents a promising setup to measure both ENA features on local scales at low altitudes, providing information on cusps and locations of restricted precipitation, as well as the total emission on a global level, especially from the MMO orbiter. Together with a model like our SDTrimSP-3D regolith simulations, it will then be possible to constrain the ion fluxes to the surface as well as their impact energies. These measurements will contribute to improving the understanding of Mercury's magnetosphere and its interaction with the surface. This will in turn significantly help in constraining contributions to the surface-bound exosphere from sputtering by ion impacts. Furthermore, detailed analysis of ENA properties such as the reflection coefficients and angular scattering functions might allow constraints on regolith properties such as the porosity.

While the current model presented in this section assumes that backscattering is the same on Mercury as the Moon, there exist several uncertainties about Mercury's regolith that could affect the ENA emission. For example, different porosities, grain shapes, grain size distributions and compositions are expected or at least possible (Langevin, 1997; Gundlach & Blum, 2013) and their influence on the backscattering of solar wind protons in a complex environment such as the ion-surface interaction of Mercury should be further investigated. This would represent an important step towards establishing ENA measurements as a tool to constrain a range of surface properties on planetary bodies like Mercury that are currently only accessible via remote observation.

6 Conclusions

In this study, we discussed the modeling of ENA emission from atmosphereless rocky bodies, in particular the Moon and Mercury, by simulating solar wind proton impacts and backscattering from regolith grains in the SDTrimSP-3D code. After previously studying the total backscattering and its dependence on regolith porosity, we have now inves-

tigated scattering angles and energies to explain ENA characteristics observed at the Moon. In doing so, we have shown that the model successfully reproduces the most important observations of ENA characteristics. Dominant backward ENA emission towards the Sun, previously observed with the Chandrayaan-1 orbiter, is prevalent in the simulations and can be connected to the geometry of the porous regolith structure. This leads to preferential impacts on sun-facing areas of the grains, while other regions are shadowed and the backward emission is a result of the larger available solid angle in this direction. In contrast, the effect of the regolith on the scattering energies was found to be smaller, in part due to the previous measurement selection criteria of only studying ENAs emitted around the zenith direction. Instead our simulations show that the energy of the precipitating protons is the main driver for ENA energy spectra. This agrees with previous Chandrayaan-1 measurements that showed significant correlation between ENA energies and solar wind parameters. For different solar wind velocities, we also calculated the global lunar ENA albedo. Both the albedo's absolute value as well as its decrease from about 0.2 at slow solar wind velocities to around 0.1 for the faster solar wind coincide well for the SDTrimSP-3D simulations and the IBEX data. The decrease is generally related to an increased proton range in the solid, while the regolith structure determines the albedo's absolute value.

Some aspects of the simulations of ENA emission characteristics are not yet in full agreement with ENA measurements, in particular the width of the angular scattering function and the mean ENA energy for fast solar wind velocities. Further studies, both from the experimental and the modeling side will be necessary to enhance the model precision in these regards. This includes potential improvement in the fundamental inputs SDTrimSP-3D uses to simulate the ion-solid interaction, as well as more detailed consideration of regolith characteristics such as grain shapes or grain size distributions up to features such as larger-scale slopes on the lunar surface.

The overall agreement between ENA measurements and the simulations is still very good and based on this, we modeled the ENA fluxes around the Moon and Mercury. In contrast to the rather simple image around the Moon, precipitation conditions in Mercury's magnetosphere are more structured and variable and this is mirrored in the ENA emission. We explored this aspect using two cases from Mercury hybrid plasma models as an ion precipitation input, showing the response of the ENA fluxes to changing upstream solar wind conditions. Corresponding to the regions with favored precipita-

tion, the main ENA flux features are predicted to be observed above the polar cusps as well as the nightside. Especially the nightside ENA emission can be expected to change significantly, but this also shows the promise of using ENA measurements as a precipitation monitor. In this context, the asymmetric polar orbits of the BepiColombo spacecraft will nicely allow the measurement of ENAs at different distances, allowing insights into both local and global ion precipitation. A wide range of ENA measurements combined with simulation studies such as our SDTrimSP-3D regolith model will then also be useful to constrain surface parameters such as the porosity. We are confident that these efforts will act as a helpful addition to other remote analysis technique for improving our understanding of Mercury's surface and its interaction with the surrounding plasma environment.

Open Research

The research data presented in this manuscript is included in the accompanying dataset uploaded on Figshare (Szabo et al., 2023). Licenses of SDTrimSP and SDTrimSP-3D can be acquired by contacting `sdtrimsp@ipp.mpg.de` or the Max-Planck-Innovation GmbH. The SDTrimSP graphical user interface is available on github (Szabo, Weichselbaum, et al., 2022b).

Acknowledgments

The authors gratefully acknowledge support from NASA's Solar System Research Virtual Institute (SSERVI) via the LEADER team, grant #80NSSC20M0060, as well as support from the Swedish National Space Agency, grant 2022-00183.

References

Alberti, T., Sun, W., Varsani, A., Heyner, D., Orsini, S., Milillo, A., ... others (2023). High-energy particle enhancements in the solar wind upstream Mercury during the first BepiColombo flyby: SERENA/PICAM and MPO-MAG observations. *Astronomy & Astrophysics*, *669*, A35.

Allegrini, F., Dayeh, M., Desai, M., Funsten, H., Fuselier, S., Janzen, P., ... others (2013). Lunar energetic neutral atom (ENA) spectra measured by the interstellar boundary explorer (IBEX). *Planetary and space science*, *85*, 232–242.

Baumjohann, W., & Treumann, R. A. (2012). *Basic Space Plasma Physics*. World

Scientific.

Behrisch, R., & Eckstein, W. (2007). *Sputtering by particle bombardment: experiments and computer calculations from threshold to MeV energies* (Vol. 110). Springer Science & Business Media.

Beikler, R., & Taglauer, E. (2001). Trajectory resolved analysis of LEIS energy spectra: Neutralization and surface structure. *Nuclear Instruments and Methods in Physics Research Section B: Beam Interactions with Materials and Atoms*, *182*(1-4), 180–186.

Benkhoff, J., Murakami, G., Baumjohann, W., Besse, S., Bunce, E., Casale, M., ... others (2021). BepiColombo-mission overview and science goals. *Space Science Reviews*, *217*(8), 90.

Benkhoff, J., Van Casteren, J., Hayakawa, H., Fujimoto, M., Laakso, H., Novara, M., ... Ziethe, R. (2010). BepiColombo — Comprehensive exploration of Mercury: Mission overview and science goals. *Planetary and Space Science*, *58*(1-2), 2–20.

Benna, M., Anderson, B. J., Baker, D. N., Boardsen, S. A., Gloeckler, G., Gold, R. E., ... others (2010). Modeling of the magnetosphere of Mercury at the time of the first MESSENGER flyby. *Icarus*, *209*(1), 3–10.

Bissbort, T., Jiang, Q., Becker, H.-W., Foteinou, V., & Chakraborty, S. (2023). An experimental study of proton implantation in olivine. *Physics and Chemistry of Minerals*, *50*(2), 1–10.

Chaufray, J.-Y., Quémerais, E., Koutroumpa, D., Robidel, R., Leblanc, F., Reberac, A., ... others (2023). The EUV reflectance of Mercury's surface measured by BepiColombo/PHEBUS. *Journal of Geophysical Research: Planets*, e2022JE007669.

Christoph, J., Minesinger, G., Bu, C., Dukes, C., & Elkins-Tanton, L. (2022). Space weathering effects in troilite by simulated solar-wind hydrogen and helium ion irradiation. *Journal of Geophysical Research: Planets*, e2021JE006916.

Correa, A. A. (2018). Calculating electronic stopping power in materials from first principles. *Computational Materials Science*, *150*, 291–303.

Cupak, C., Szabo, P. S., Biber, H., Stadlmayr, R., Grave, C., Fellinger, M., ... others (2021). Sputter yields of rough surfaces: Importance of the mean surface inclination angle from nano-to microscopic rough regimes. *Applied Surface*

Science, *570*, 151204.

Deniau, A., Nénon, Q., André, N., Mazelle, C., Rahmati, A., Fowler, C., ... Penou, E. (2022). MAVEN Proton Observations Near the Martian Moon Phobos: Does Phobos Backscatter Solar Wind Protons? *Geophysical Research Letters*, *49*(23), e2022GL101014.

Domingue, D. L., Chapman, C. R., Killen, R. M., Zurbuchen, T. H., Gilbert, J. A., Sarantos, M., ... others (2014). Mercury's weather-beaten surface: Understanding Mercury in the context of lunar and asteroidal space weathering studies. *Space Science Reviews*, *181*, 121–214.

Fatemi, S., Poppe, A., & Barabash, S. (2020). Hybrid simulations of solar wind proton precipitation to the surface of Mercury. *Journal of Geophysical Research: Space Physics*, *125*(4), e2019JA027706.

Funsten, H., Allegrini, F., Bochsler, P., Fuselier, S., Gruntman, M., Henderson, K., ... others (2013). Reflection of solar wind hydrogen from the lunar surface. *Journal of Geophysical Research: Planets*, *118*(2), 292–305.

Futaana, Y., Barabash, S., Holmström, M., Fedorov, A., Nilsson, H., Lundin, R., ... Fränz, M. (2010). Backscattered solar wind protons by Phobos. *Journal of Geophysical Research: Space Physics*, *115*(A10).

Futaana, Y., Barabash, S., Wieser, M., Holmström, M., Lue, C., Wurz, P., ... Asamura, K. (2012). Empirical energy spectra of neutralized solar wind protons from the lunar regolith. *Journal of Geophysical Research: Planets*, *117*(E5).

Futaana, Y., Barabash, S., Wieser, M., Lue, C., Wurz, P., Vorburger, A., ... Asamura, K. (2013). Remote energetic neutral atom imaging of electric potential over a lunar magnetic anomaly. *Geophysical Research Letters*, *40*(2), 262–266.

Futaana, Y., Holmström, M., Fedorov, A., & Barabash, S. (2021). Does Phobos Reflect Solar Wind Protons? Mars Express Special Flyby Operations With and Without the Presence of Phobos. *Journal of Geophysical Research: Planets*, *126*(11), e2021JE006969.

Glass, A., Raines, J., Jia, X., Sun, W., Imber, S., Dewey, R., & Slavin, J. (2022). Observations of Mercury's Plasma Sheet Horn: Characterization and Contribution to Proton Precipitation. *Journal of Geophysical Research: Space Physics*,

127(12), e2022JA030969.

Goebl, D., Roth, D., & Bauer, P. (2013). Role of d electrons in electronic stopping of slow light ions. *Physical Review A*, *87*(6), 062903.

Gundlach, B., & Blum, J. (2013). A new method to determine the grain size of planetary regolith. *Icarus*, *223*(1), 479–492.

Hapke, B., Nelson, R., & Smythe, W. (1998). The opposition effect of the moon: Coherent backscatter and shadow hiding. *Icarus*, *133*(1), 89–97.

Hapke, B., & Sato, H. (2016). The porosity of the upper lunar regolith. *Icarus*, *273*, 75–83.

Harada, Y., Aizawa, S., Saito, Y., André, N., Persson, M., Delcourt, D., ... others (2022). BepiColombo Mio Observations of Low-Energy Ions During the First Mercury Flyby: Initial Results. *Geophysical Research Letters*, *49*(17), e2022GL100279.

Harada, Y., Futaana, Y., Barabash, S., Wieser, M., Wurz, P., Bhardwaj, A., ... others (2014). Backscattered energetic neutral atoms from the Moon in the Earth's plasma sheet observed by Chandarayaan-1/Sub-keV atom reflecting analyzer instrument. *Journal of Geophysical Research: Space Physics*, *119*(5), 3573–3584.

Helfenstein, P., Veverka, J., & Hillier, J. (1997). The lunar opposition effect: A test of alternative models. *Icarus*, *128*(1), 2–14.

Herčík, D., Trávníček, P. M., Štverák, Š., & Hellinger, P. (2016). Properties of Hermean plasma belt: Numerical simulations and comparison with MESSENGER data. *Journal of Geophysical Research: Space Physics*, *121*(1), 413–431.

Hlawacek, G., Veligura, V., van Gastel, R., & Poelsema, B. (2014). Helium ion microscopy. *Journal of Vacuum Science & Technology B, Nanotechnology and Microelectronics: Materials, Processing, Measurement, and Phenomena*, *32*(2), 020801.

Hodges, R. (2011). Resolution of the lunar hydrogen enigma. *Geophysical Research Letters*, *38*(6).

Jäggi, N., Mutzke, A., Biber, H., Brötzner, J., Szabo, P. S., Aumayr, F., ... Galli, A. (2023). New compound and hybrid binding energy sputter model for modeling purposes in agreement with experimental data. *The Planetary Science Journal*, *4*(5), 86.

Kallio, E., & Janhunen, P. (2003). Solar wind and magnetospheric ion impact on mercury's surface. *Geophysical Research Letters*, *30*(17).

Kazama, Y. (2006). *Simulation report of the ENA instrument.* Swedish Institute of Space Physics.

Kazama, Y., Barabash, S., Wieser, M., Asamura, K., & Wurz, P. (2007). Development of an LENA instrument for planetary missions by numerical simulations. *Planetary and Space Science*, *55*(11), 1518–1529.

Killen, R. M., Cremonese, G., Lammer, H., Orsini, S., Potter, A. E., Sprague, A. L., ... others (2007). Processes that promote and deplete the exosphere of Mercury. *Space Science Reviews*, *132*, 433–509.

Killen, R. M., Morrissey, L. S., Burger, M. H., Vervack, R. J., Tucker, O. J., & Savin, D. W. (2022). The Influence of Surface Binding Energy on Sputtering in Models of the Sodium Exosphere of Mercury. *The Planetary Science Journal*, *3*(6), 139.

King, J., & Papitashvili, N. (2005). Solar wind spatial scales in and comparisons of hourly Wind and ACE plasma and magnetic field data. *Journal of Geophysical Research: Space Physics*, *110*(A2).

Kulchitsky, A. V., Hurley, D. M., Johnson, J. B., Duvoy, P. X., & Zimmerman, M. (2018). Solar wind access to grains in the upper layer of regolith. *Journal of Geophysical Research: Planets*, *123*(4), 972–981.

Kuramoto, K., Kawakatsu, Y., Fujimoto, M., Araya, A., Barucci, M. A., Genda, H., ... others (2022). Martian moons exploration MMX: sample return mission to Phobos elucidating formation processes of habitable planets. *Earth, Planets and Space*, *74*(1), 1–31.

Langevin, Y. (1997). The regolith of Mercury: present knowledge and implications for the Mercury Orbiter mission. *Planetary and space science*, *45*(1), 31–37.

Leblanc, F., Deborde, R., Tramontina, D., Bringa, E., Chaufray, J.-Y., Aizawa, S., ... others (2023). On the origins of backscattered solar wind energetic neutral hydrogen from the Moon and Mercury. *Planetary and Space Science*, *229*, 105660.

Lopez, R. E., & Freeman, J. W. (1986). Solar wind proton temperature-velocity relationship. *Journal of Geophysical Research: Space Physics*, *91*(A2), 1701–1705.

Lue, C., Futaana, Y., Barabash, S., Saito, Y., Nishino, M., Wieser, M., ... Wurz, P. (2016). Scattering characteristics and imaging of energetic neutral atoms from the Moon in the terrestrial magnetosheath. *Journal of Geophysical Research: Space Physics*, *121*(1), 432–445.

Lue, C., Futaana, Y., Barabash, S., Wieser, M., Bhardwaj, A., & Wurz, P. (2014). Chandrayaan-1 observations of backscattered solar wind protons from the lunar regolith: Dependence on the solar wind speed. *Journal of Geophysical Research: Planets*, *119*(5), 968–975.

Lue, C., Futaana, Y., Barabash, S., Wieser, M., Bhardwaj, A., Wurz, P., & Asamura, K. (2017). Solar wind scattering from the surface of Mercury: Lessons from the Moon. *Icarus*, *296*, 39–48.

Lue, C., Futaana, Y., Barabash, S., Wieser, M., Holmström, M., Bhardwaj, A., ... Wurz, P. (2011). Strong influence of lunar crustal fields on the solar wind flow. *Geophysical Research Letters*, *38*(3).

Lue, C., Halekas, J., Poppe, A., & McFadden, J. (2018). ARTEMIS observations of solar wind proton scattering off the lunar surface. *Journal of Geophysical Research: Space Physics*, *123*(7), 5289–5299.

McComas, D., Allegrini, F., Bochsler, P., Frisch, P., Funsten, H., Gruntman, M., ... others (2009). Lunar backscatter and neutralization of the solar wind: First observations of neutral atoms from the Moon. *Geophysical Research Letters*, *36*(12).

Morrissey, L. S., Schaible, M. J., Tucker, O. J., Szabo, P. S., Bacon, G., Killen, R. M., & Savin, D. W. (2023). Establishing a best practice for sdtrimsp simulations of solar wind ion sputtering. *The Planetary Science Journal*, *4*(4), 67.

Morrissey, L. S., Tucker, O. J., Killen, R. M., Nakhla, S., & Savin, D. W. (2022). Solar Wind Ion Sputtering of Sodium from Silicates Using Molecular Dynamics Calculations of Surface Binding Energies. *The Astrophysical Journal Letters*, *925*(1), L6.

Mutzke, A., Schneider, R., Eckstein, W., Dohmen, R., Schmid, K., Toussaint, U. v., & Badelow, G. (2019). SDTrimSP Version 6.00.

Niehus, H., Heiland, W., & Taglauer, E. (1993). Low-energy ion scattering at surfaces. *Surface Science Reports*, *17*(4-5), 213–303.

Orsini, S., Livi, S., Lichtenegger, H., Barabash, S., Milillo, A., De Angelis, E., ... others (2021). SERENA: particle instrument suite for determining the Sun-Mercury interaction from BepiColombo. *Space science reviews*, *217*(1), 1–107.

Orsini, S., Milillo, A., Lichtenegger, H., Varsani, A., Barabash, S., Livi, S., ... others (2022). Inner southern magnetosphere observation of mercury via serena ion sensors in bepicolombo mission. *Nature Communications*, *13*(1), 7390.

Pfleger, M., Lichtenegger, H., Wurz, P., Lammer, H., Kallio, E., Alho, M., ... Martín-Fernández, J. (2015). 3D-modeling of Mercury's solar wind sputtered surface-exosphere environment. *Planetary and Space Science*, *115*, 90–101.

Pieters, C. M., & Noble, S. K. (2016). Space weathering on airless bodies. *Journal of Geophysical Research: Planets*, *121*(10), 1865–1884.

Poppe, A., Halekas, J., & Harada, Y. (2022). A comprehensive model for pickup ion formation at the Moon. *Journal of Geophysical Research: Planets*, *127*(10), e2022JE007422.

Raines, J. M., Dewey, R. M., Staudacher, N. M., Tracy, P. J., Bert, C. M., Sarantos, M., ... others (2022). Proton precipitation in mercury's northern magnetospheric cusp. *Journal of Geophysical Research: Space Physics*, *127*(11), e2022JA030397.

Rodriguez M., D., Saul, L., Wurz, P., Fuselier, S., Funsten, H., McComas, D., ... others (2012). IBEX-Lo observations of energetic neutral hydrogen atoms originating from the lunar surface. *Planetary and space science*, *60*(1), 297–303.

Roth, D., Bruckner, B., Undeutsch, G., Paneta, V., Mardare, A., McGahan, C., ... others (2017). Electronic stopping of slow protons in oxides: scaling properties. *Physical Review Letters*, *119*(16), 163401.

Saito, Y., Delcourt, D., Hirahara, M., Barabash, S., André, N., Takashima, T., ... others (2021). Pre-flight calibration and near-earth commissioning results of the Mercury Plasma Particle Experiment (MPPE) onboard MMO (Mio). *Space Science Reviews*, *217*(5), 1–91.

Saito, Y., Sauvaud, J., Hirahara, M., Barabash, S., Delcourt, D., Takashima, T., ... others (2010). Scientific objectives and instrumentation of Mercury Plasma Particle Experiment (MPPE) onboard MMO. *Planetary and Space Science*, *58*(1-2), 182–200.

Saito, Y., Yokota, S., Tanaka, T., Asamura, K., Nishino, M., Fujimoto, M., ... oth-

ers (2008). Solar wind proton reflection at the lunar surface: Low energy ion measurement by MAP-PACE onboard SELENE (KAGUYA). *Geophysical Research Letters*, *35*(24).

Sarantos, M., Killen, R. M., & Kim, D. (2007). Predicting the long-term solar wind ion-sputtering source at mercury. *Planetary and Space Science*, *55*(11), 1584–1595.

Schaible, M., Dukes, C., Hutcherson, A., Lee, P., Collier, M., & Johnson, R. (2017). Solar wind sputtering rates of small bodies and ion mass spectrometry detection of secondary ions. *Journal of Geophysical Research: Planets*, *122*(10), 1968–1983.

Schaufelberger, A., Wurz, P., Barabash, S., Wieser, M., Futaana, Y., Holmström, M., ... Asamura, K. (2011). Scattering function for energetic neutral hydrogen atoms off the lunar surface. *Geophysical Research Letters*, *38*(22).

Schriver, D., Trávníček, P. M., Anderson, B. J., Ashour-Abdalla, M., Baker, D. N., Benna, M., ... others (2011). Quasi-trapped ion and electron populations at Mercury. *Geophysical Research Letters*, *38*(23).

Shams-Latifi, J., Ström, P., Pitthan, E., & Primetzhofer, D. (2022). An in-situ ToF-LEIS and AES study of near-surface modifications of the composition of EUROFER97 induced by thermal annealing. *Nuclear Materials and Energy*, *30*, 101139.

Slavin, J. A., Acuña, M. H., Anderson, B. J., Baker, D. N., Benna, M., Gloeckler, G., ... others (2008). Mercury's magnetosphere after MESSENGER's first flyby. *Science*, *321*(5885), 85–89.

Solomon, S. C., Nittler, L. R., & Anderson, B. J. (2018). *Mercury: The view after MESSENGER* (Vol. 21). Cambridge University Press.

Strom, R. G. (1979). Mercury-A post-Mariner 10 assessment. *Space Science Reviews*, *24*, 3–70.

Szabo, P. S., Biber, H., Jäggi, N., Brenner, M., Weichselbaum, D., Niggas, A., ... Aumayr, F. (2020). Dynamic potential sputtering of lunar analog material by solar wind ions. *The Astrophysical Journal*, *891*(1), 100.

Szabo, P. S., Cupak, C., Biber, H., Jäggi, N., Galli, A., Wurz, P., & Aumayr, F. (2022). Analytical model for the sputtering of rough surfaces. *Surfaces and Interfaces*, *30*, 101924.

Szabo, P. S., Poppe, A. R., Biber, H., Mutzke, A., Pichler, J., Jäggi, N., ... Aumayr, F. (2022). Deducing lunar regolith porosity from energetic neutral atom emission. *Geophysical Research Letters*, *49*(21), e2022GL101232.

Szabo, P. S., Poppe, A. R., Mutzke, A., Fatemi, S., Vorburger, A., & Wurz, P. (2023). *Energetic Neutral Atom (ENA) emission characteristics at the Moon and Mercury from 3D regolith simulations of solar wind reflection (Dataset).* Retrieved from `https://doi.org/10.6084/m9.figshare.22826228` doi: 10.6084/m9.figshare.22826228

Szabo, P. S., Weichselbaum, D., Biber, H., Cupak, C., Mutzke, A., Wilhelm, R., & Aumayr, F. (2022a). Graphical user interface for SDTrimSP to simulate sputtering, ion implantation and the dynamic effects of ion irradiation. *Nuclear Instruments and Methods in Physics Research Section B: Beam Interactions with Materials and Atoms*, *522*, 47–53.

Szabo, P. S., Weichselbaum, D., Biber, H., Cupak, C., Mutzke, A., Wilhelm, R., & Aumayr, F. (2022b). *SDTrimSP GUI (Software).* Retrieved from `https://github.com/psszabo/SDTrimSP-GUI`

Tran, T. T., Jablonka, L., Bruckner, B., Rund, S., Roth, D., Sortica, M. A., ... Primetzhofer, D. (2019). Electronic interaction of slow hydrogen and helium ions with nickel-silicon systems. *Physical Review A*, *100*(3), 032705.

Tucker, O., Farrell, W., Killen, R., & Hurley, D. (2019). Solar wind implantation into the lunar regolith: Monte Carlo simulations of H retention in a surface with defects and the H2 exosphere. *Journal of Geophysical Research: Planets*, *124*(2), 278–293.

Varela, J., Pantellini, F., & Moncuquet, M. (2015). The effect of interplanetary magnetic field orientation on the solar wind flux impacting Mercury's surface. *Planetary and Space Science*, *119*, 264–269.

Von Toussaint, U., Mutzke, A., & Manhard, A. (2017). Sputtering of rough surfaces: a 3D simulation study. *Physica Scripta*, *2017*(T170), 014056.

Vorburger, A., Wurz, P., Barabash, S., Futaana, Y., Wieser, M., Bhardwaj, A., ... Asamura, K. (2016). Transport of solar wind plasma onto the lunar nightside surface. *Geophysical Research Letters*, *43*(20), 10–586.

Vorburger, A., Wurz, P., Barabash, S., Wieser, M., Futaana, Y., Bhardwaj, A., & Asamura, K. (2015). Imaging the South Pole–Aitken basin in backscattered

neutral hydrogen atoms. *Planetary and Space Science*, *115*, 57–63.

Vorburger, A., Wurz, P., Barabash, S., Wieser, M., Futaana, Y., Holmström, M., ... Asamura, K. (2012). Energetic neutral atom observations of magnetic anomalies on the lunar surface. *Journal of Geophysical Research: Space Physics*, *117*(A7).

Vorburger, A., Wurz, P., Barabash, S., Wieser, M., Futaana, Y., Lue, C., ... Asamura, K. (2013). Energetic neutral atom imaging of the lunar surface. *Journal of Geophysical Research: Space Physics*, *118*(7), 3937–3945.

Wang, H., Xiao, C., Shi, Q., Guo, R., Yue, C., Xie, L., ... others (2021). Energetic neutral atom distribution on the lunar surface and its relationship with solar wind conditions. *The Astrophysical Journal Letters*, *922*(2), L41.

Wei, D., Wang, J., Nie, J., & Zhou, B. (2018). Generation of realistic sand particles with fractal nature using an improved spherical harmonic analysis. *Computers and Geotechnics*, *104*, 1–12.

Wieser, M., Barabash, S., Futaana, Y., Holmström, M., Bhardwaj, A., Sridharan, R., ... Asamura, K. (2009). Extremely high reflection of solar wind protons as neutral hydrogen atoms from regolith in space. *Planetary and Space Science*, *57*(14-15), 2132–2134.

Wieser, M., Barabash, S., Futaana, Y., Holmström, M., Bhardwaj, A., Sridharan, R., ... Asamura, K. (2010). First observation of a mini-magnetosphere above a lunar magnetic anomaly using energetic neutral atoms. *Geophysical Research Letters*, *37*(5).

Winslow, R. M., Johnson, C. L., Anderson, B. J., Gershman, D. J., Raines, J. M., Lillis, R. J., ... others (2014). Mercury's surface magnetic field determined from proton-reflection magnetometry. *Geophysical Research Letters*, *41*(13), 4463–4470.

Wurz, P., Fatemi, S., Galli, A., Halekas, J., Harada, Y., Jäggi, N., ... others (2022). Particles and photons as drivers for particle release from the surfaces of the Moon and Mercury. *Space Science Reviews*, *218*(3), 1–83.

Wurz, P., Rohner, U., Whitby, J. A., Kolb, C., Lammer, H., Dobnikar, P., & Martín-Fernández, J. (2007). The lunar exosphere: The sputtering contribution. *Icarus*, *191*(2), 486–496.

Yokota, S., Terada, N., Matsuoka, A., Murata, N., Saito, Y., Delcourt, D., ... others

(2021). In situ observations of ions and magnetic field around Phobos: the mass spectrum analyzer (MSA) for the Martian Moons eXploration (MMX) mission. *Earth, Planets and Space*, *73*(1), 1–18.